npj computational materials

www.nature.com/npjcompumats

ARTICLE OPEN

Check for updates

$LaBr_2$ bilayer multiferroic moiré superlattice with robust magnetoelectric coupling and magnetic bimerons

Wei Sun[1,3], Wenxuan Wang[1,3], Hang Li[1]✉, Xiaoning Li[2], Zheyin Yu[2], Ying Bai[1], Guangbiao Zhang[1] and Zhenxiang Cheng[2]✉

Two-dimensional (2D) van der Waals (vdW) materials provide the versatile playground to stack two or more vdW layers for creation of superior materials with desired properties. Here we theoretically adopt a twisted stack-engineering of two $LaBr_2$ monolayers to break space inversion symmetry for ferroelectricity and ultimately multiferroism. The enhancement and reversal of electric polarization are accompanied with the transition from interlayer ferromagnetic and antiferromagnetic orderings, demonstrating an effective magnetoelectric coupling effect with a mechanism dissimilar to that of the conventional multiferroics. Magnetization dynamics simulations show that such magnetic phase transition can excite topologically protected bimeron, and the skyrmion Hall effect can be suppressed by bilayer-bimeron stabilized in both ferromagnetic and antiferromagnetic configurations. Moreover, in the small-angle twisted moiré superlattice, the uniform polarization will evolve into a staggered domain structure, accompanied with the appearance of bimeron, which forms a significant discrepancy with the non-twisted stack-engineered multiferroic $LaBr_2$ bilayer. This work provides a strategy for 2D multiferroic materials by twisted stack engineering of magnetic single layers.

npj Computational Materials (2022)8:159 ; https://doi.org/10.1038/s41524-022-00833-4

INTRODUCTION

Multiferroic materials with robust magnetoelectric coupling is highly attractive with significant applications prospect in the field of spintronics and electronics such as high density and low energy consuming nonvolatile memories and high sensitivity sensors[1,2]. However, the basic contradiction between the required empty *d*-electron configuration of the conventional ferroelectric (FE) phase and the partially filled *d* orbit demanded for the traditional magnetic phase, results in the scarcity of single phase multiferroic material with coexistence of the two different ferric properties[3,4].

The successful exfoliation of graphene[5], has led to revolution in discovering two-dimensional (2D) van der Waals (vdW) materials with superior physical properties as well as revolution in materials engineering[6–11]. This allows multiferroics to be achieved by simply stacking of ferromagnetic (FM) and FE monolayers to form heterostructure (HS). Such 2D multiferroic HS has shown strong magnetoelectric coupling, i.e, nonvolatile control of long-range magnetic ordering as well as topologically nontrivial spin textures by FE polarization[12–16]. However, the limited availability of individual 2D FM and 2D FE materials hinder the stacking of 2D FM and 2D FE for 2D multiferroic HS. Furthermore, the asymmetric interfacial coupling in this type of 2D HS may seriously distort the FE double-well potential, thus destabilizing the ferroelectricity and causing the failure of stacking strategy[17].

The recent vdW stack engineering of simple non-polar single layers to break the space inversion symmetry through the relative twisting between layers to induce out-of-plane polarization, has revolutionized the design 2D FE HS materials[18]. For example, the spontaneous out-of-plane ferroelectric polarization in stacked WTe_2 bilayer and BN bilayer can be reversed upon interlayer sliding of an in-plane translation by an external electric field[19–21]. As the polarization in the stacked bilayers is caused by interlayer stacking, the rule for empty *d* for ferroelectricity are not applied, which can eliminate the contradiction for the FM and FE coexisting. The stacking induced ferroelectric polarization can be applied to construct 2D vdW multiferroic materials[22]. By twisted stacking 2D vdW magnetic bilayer, ferroelectric polarization can be induced, while the system will remain magnetic due to the existing of transition metal elements. The expected coexisting of ferroelectric polarization and magnetism will enable the system multiferroic. In addition, stacking of the identical materials can effectively address the potential ferroelectric damage due to asymmetric interface coupling in FM/FE HS.

The topological magnetic state with whirling spin configuration has attracted great interest in 2D materials. The topology protection and transport properties endow those topological magnetic states with great advantages in serving as information carriers for next-generation information storage and processing devices[23–26]. Those topological spin configurations can be strongly affected by the magnetic anisotropy in 2D magnets. Particularly, magnetic skyrmion emerges in easy-axis magnets while bimeron in easy-plane magnets[27–32]. Furthermore, by integrating with 2D vdW multiferroic materials, topological spin textures can be intriguingly tuned by polarization reversal, allowing skyrmion-based devices in atom-thick level with extreme low energy consumption[15,16].

Atomically thin layers of 2D materials can be assembled in vertical stacking, where their strong covalent bonds provide the in-plane stability, and the relatively weak vdW-like forces hold the advantage of easy-stacking[8,9], enabling coupling between monolayer crystals with incommensurate lattices and arbitrary mutual rotation. When single layers of 2D materials are stacked on top of one another with a small twist in orientation, the way of layers stacked will change periodically and smoothly over long range, and the resulting periodic moiré superlattices defines a different length and energy scale[33–35], which offers an additional degree of freedom for tuning material properties. For example, exotic and relevant physical phenomena, such as Mott insulators and

[1]International Joint Research Laboratory of New Energy Materials and Devices of Henan Province, School of Physics and Electronics, Henan University, Kaifeng 475004, P. R. China. [2]Institute for Superconducting & Electronic Materials, Australian Institute of Innovative Materials, University of Wollongong, Innovation Campus, Squires Way, North Wollongong, NSW 2500, Australia. [3]These authors contributed equally: Wei Sun, Wenxuan Wang. ✉email: hang.li@vip.henu.edu.cn; cheng@uow.edu.au

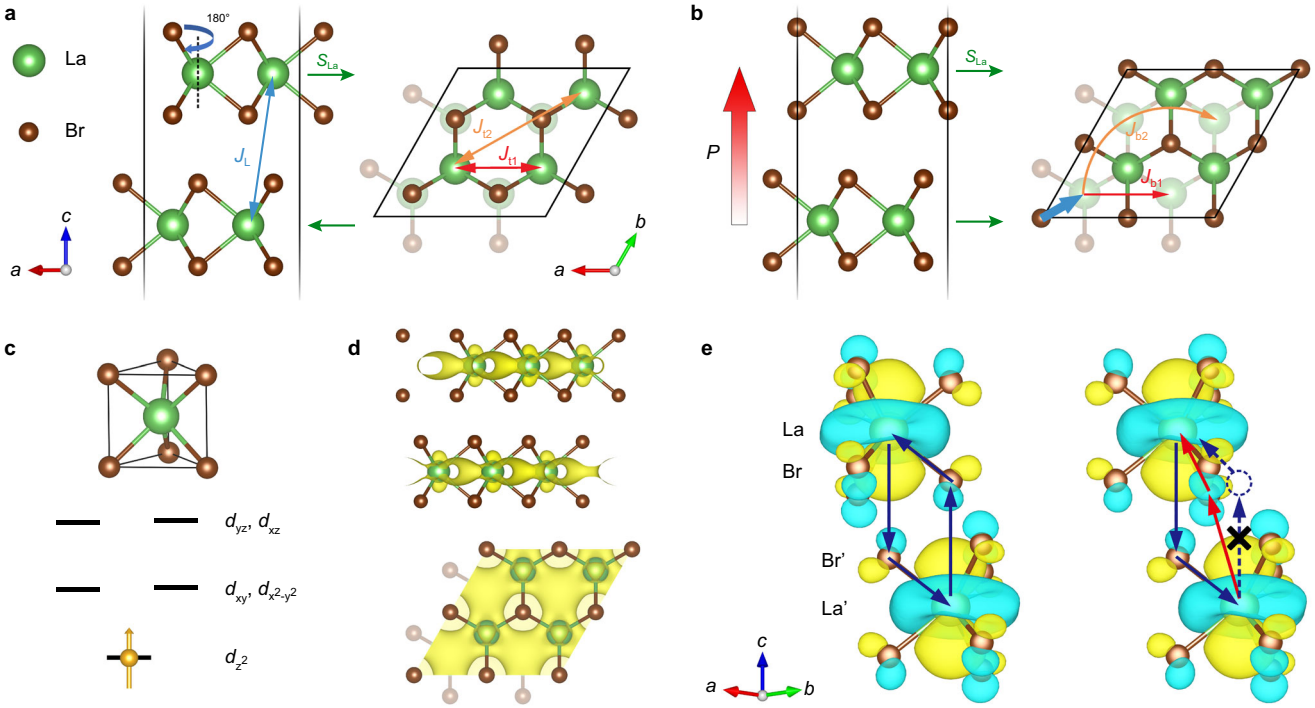

Fig. 1 The lattice structure of bilayer $LaBr_2$. **a**, **b** show both the side and top views of 2*H*- and 3*R*-type stacking, respectively. S_{La} represents the spin direction of La ions in upper and lower layer. **c** The splitting of 5*d* orbitals for La^{2+} in the trigonal prismatic crystal field. **d** Spin density for 3 *R* $LaBr_2$ bilayer. **e** The maximally localized Wannier of La-$5d_z^2$ states for 2*H* and 3 *R* type. Yellow and cyan colors represent positive and negative, respectively, isovalue surfaces of the Wannier function. The red and blue arrows represent FM and AFM superexchange paths between different atoms, respectively.

unconventional superconductivity, have recently been observed in twisted graphene with small magic angles[36–38]. For 2D bilayer magnets, such a long-period lateral modulation of spatial change of the stacking order can be available for controlling of interlayer exchange coupling and spatial symmetry[39–41], which gives rise to strong coupling between magnetism and polarization through interlayer interactions.

In this work, we investigated non-twisted (3 *R* stacking) and 180° twisted (2*H* stacking) stacking configurations of magnetic $LaBr_2$ bilayers, which were subsequently extended to the entire moiré pattern with smooth variations in local stacking at small twisting angles. Through our density functional theory (DFT) calculations, we demonstrate that the different stacking types of 2*H* and 3 *R* exhibit antiferromagnetic (AFM) and FM states, respectively (as shown in Fig. 1a, b). In addition, 3 *R* stacking induces an out-of-plane spontaneous polarization, and a strong magnetoelectric coupling effect occurs in this type, we designate it as stacking-engineered multiferroics. In 3 *R* type $LaBr_2$ bilayer, the enhancement and reversal of ferroelectric polarization will trigger magnetic phase transition. Spin dynamics simulations show that this can excite topologically protected bimeron from long-range magnetic orderings, and the skyrmion Hall effect can be suppressed by bilayer-bimeron stabilized in FM or AFM configurations. In addition, for twisting 3*R*-type $LaBr_2$ bilayer at small angles, 3*R*-type stacking configurations with opposite polarization exist simultaneously in the local region of the moiré superlattice, thus leading to staggered polarization domains and magnetic bimeron stabilized in domains. This indicates that there is a significant discrepancy between non-twisted and twisted stacking-engineered 2D multiferroics. Our work paves the way for the design of 2D HS multiferroics by twisted stacking 2D VDW magnetic single layers with strong ME coupling as well as skyrmion devices.

RESULT

3 *R* stack-engineering induced multiferroicity and magnetoelectric coupling

Bulk $LaBr_2$ is a hexagonal layered crystal with a space group of $P6_3/mmc$[42]. Recently, a monolayered $LaBr_2$ has been proposed as an ideal FM semiconductor[43,44]. As shown in Fig. 1c, each La atom is trigonal prismatic coordinated to six Br atoms. Under such a condition, the 5*d* orbitals of La^{2+} split into three groups, where the lowest energy d_z^2 orbitals are filled with d^1 electrons, and giving rise to a finite magnetic moment of 1 μ_B on each La atom. The spin density distributions of 3 *R* stacking in Fig. 1d present that one part of spin density is distributed in the d_z^2 orbitals and the other is delocalized in the intralayer hexagonal cavity. The existence of such a group of La-d_z^2 orbitals, due to the weak electronegativity of La ions, enables the electrons in $LaBr_2$ more favorable to involve in interlayer coupling, serving as an ideal physical platform for the study of stacking-engineered vdW layered materials. Here, we consider two types of stacking orderings for the bilayer $LaBr_2$: 3 *R* and 2*H* stacking, see Fig. 1a, b. 2*H* type is a stacked structure consistent with the bulk that rotates the lower layer (relative to the upper layer) by 180°, which maintains the spatial inverse symmetry of the structure. In contrast, the 3 *R* type is a stacking of two $LaBr_2$ monolayers without rotation, thereby enabling the design of synthetic stacking-engineered layered multiferroic materials due to the broken space inversion symmetry. In addition, the results by DFT calculations show that the difference in stacking energy between the 2*H* and 3 *R* stacking is 0.16 meV per unit, and the very small energy difference allows both types of the $LaBr_2$ bilayer to be stable.

The stacking of vdW magnetic layers can alter heterostructure symmetry, accompanied with the further change of interlayer coupling and even the overall magnetic properties, which is exemplified by the AFM and FM ordering of CrI_3 bilayer that correspond to a high-temperature and a low-temperature

structure caused by interlayer sliding[22,45,46], respectively. For $LaBr_2$ bilayer, the related magnetism parameters, such as J and K were obtained by considering the following classical Heisenberg model for local spins:

$$H = -K\sum_i (\mathbf{m}_i \cdot \hat{\mathbf{z}})^2 - J_L \sum_{i,j} \mathbf{m}_i \cdot \mathbf{m}_j - J_{t1} \sum_{i,j} \mathbf{m}_i \cdot \mathbf{m}_j - J_{t2} \sum_{i,j} \mathbf{m}_i \cdot \mathbf{m}_j - J_{b1} \sum_{i,j} \mathbf{m}_i \cdot \mathbf{m}_j - J_{b2} \sum_{i,j} \mathbf{m}_i \cdot \mathbf{m}_j \quad (1)$$

where, $|\mathbf{m}| = 1\ \mu_B$ is the magnetic moment of La^{2+}, K is the single-ion perpendicular magnetocrystalline anisotropy arising from spin–orbital coupling, J_L is the interlayer exchange interaction, J_{t1}, J_{b1}, J_{t2}, and J_{b2} represent the nearest and the next-nearest intralayer exchange interactions in upper and lower layer respectively, as shown in Fig. 1a, b. We performed the DFT calculations of interlayer couplings for 2*H* and 3 *R* stacking phases, which are summarized in Table 1. The 2*H* type maintains the interlayer AFM exchange while the 3 *R* type possesses weak interlayer FM exchange. Through the analysis of maximally localized Wannier orbitals[47], we further show, in Fig. 1e, that the main interaction path for interlayer exchange interaction J_L in our structure is the electron hopping between La-d_z^2 and La′-d_z^2 through the La-Br′-La′ or La′-Br-La bondings. Taking La-Br′-La′ superexchange interaction as an example, the La-d_z^2 orbital forming a σ-bonding with the Br′-p_z orbital, electron can transfer from Br′-p_z to La-d_z^2 orbital and the semicovalent exchange is achieved during this process. Such a covalent component extends the cation wavefunction out over the anions to give an orbital overlapping for the superexchange electron transfer. In addition, a π-bonding between Br′-p_z and the La′-d_z^2 orbitals enable a virtual electron transfer. According to Goodenough–Kanamori–Anderson rule[48–50], La-Br′-La′ exhibits AFM superexchange. The lattice symmetry determines that the other half of the loops La′-Br-La are also AFM superexchange, resulting in a strong antiferromagnetism for 2*H*-type stacking. For 3 *R* type, the AFM superexchange of La-Br′-La′ is retained, while the broken inversion symmetry of this stacking reduces the wave function mixing of La′-Br-La exchange interaction, making La′-Br-La exhibit FM superexchange interaction. Therefore, a competition occurs in 3 *R* type between interlayer FM and AFM superexchange, which eventually manifests as weak FM coupling. The calculation of the magnetic anisotropy was also carried out for 2*H* and 3 *R* types. They both show in-plane anisotropy with a value of −24 μeV, suggesting that the interlayer configuration has little effect on the magnetic anisotropy. In addition, we performed Monte Carlo simulations based on the Heisenberg model from Eq. 1 to evaluate the phase transition temperature for 2*H* and 3 *R* type, which are 66 K and 52 K (shown in Supplementary Fig. 1), respectively, higher than that of the experimentally known phase transition temperature of CrI_3 monolayer (45 K)[51].

Calculations based on the Berry phase method, the FE polarization value P of 3 *R* stacked magnetic bilayer $LaBr_2$ is 1.16×10^{-4} C m^{-2}, which is comparable to the experimentally measured magnitude of nonmagnetic WTe_2 (3.204×10^{-4} C m^{-2} [19]) and much higher than experimental value of BN (2.25×10^{-12} C m^{-2} [18]). Similar to WTe_2 and BN bilayer, where the polarization switching by applied electric field has been experimentally achieved[18,19], the out-of-plane FE polarization of magnetic bilayer $LaBr_2$ can also be reversed by a slight interlayer sliding, as displayed by the blue arrow in Fig. 1b. By using the climbing image nudged elastic band (CI-NEB) calculations[52], we found that the FE switching should overcome an energy barrier about 14.81 meV per unit cell, as shown in Fig. 2a. In addition,

Table 1. Exchange interaction (J, in meV) and magnetocrystalline anisotropy (K, in meV) constant of 2*H*- and 3*R*-type $LaBr_2$ bilayer.

	J_L	J_{t1}	J_{t2}	J_{b1}	J_{b2}	K
2*H*-type	−0.522	8.651	−2.339	8.651	−2.339	−0.024
3*R*-type	0.018	8.897	−2.735	8.829	−2.705	−0.024

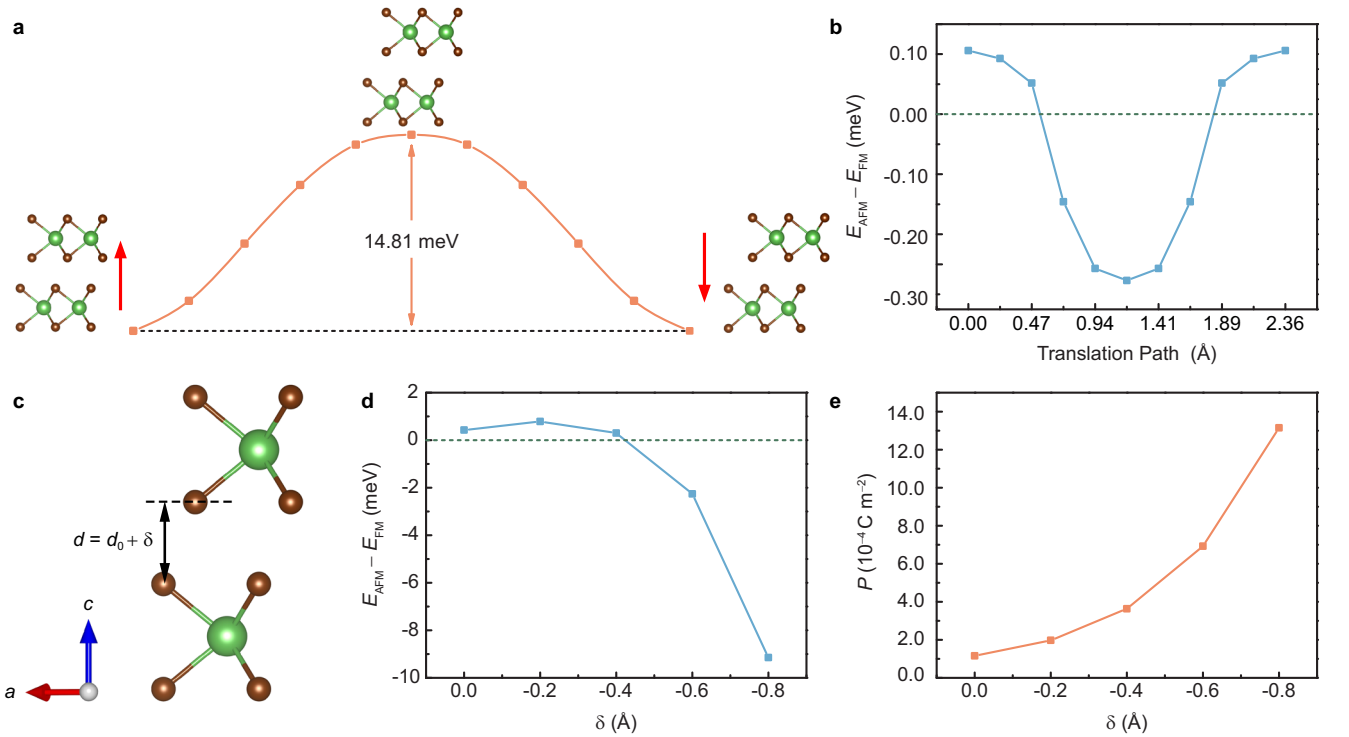

Fig. 2 Ferroelectricity and magnetism of 3 *R* $LaBr_2$ bilayer. a FE switching pathway of 3 *R* $LaBr_2$ bilayer, the red arrows denote the polarization direction. **b** Total energy difference between AFM and FM in FE switching pathway. **c** defines the distance d between two $LaBr_2$ layers. **d**, **e** Energy difference (E_{AFM}-E_{FM}) and polarization (P) are as a function of δ, respectively.

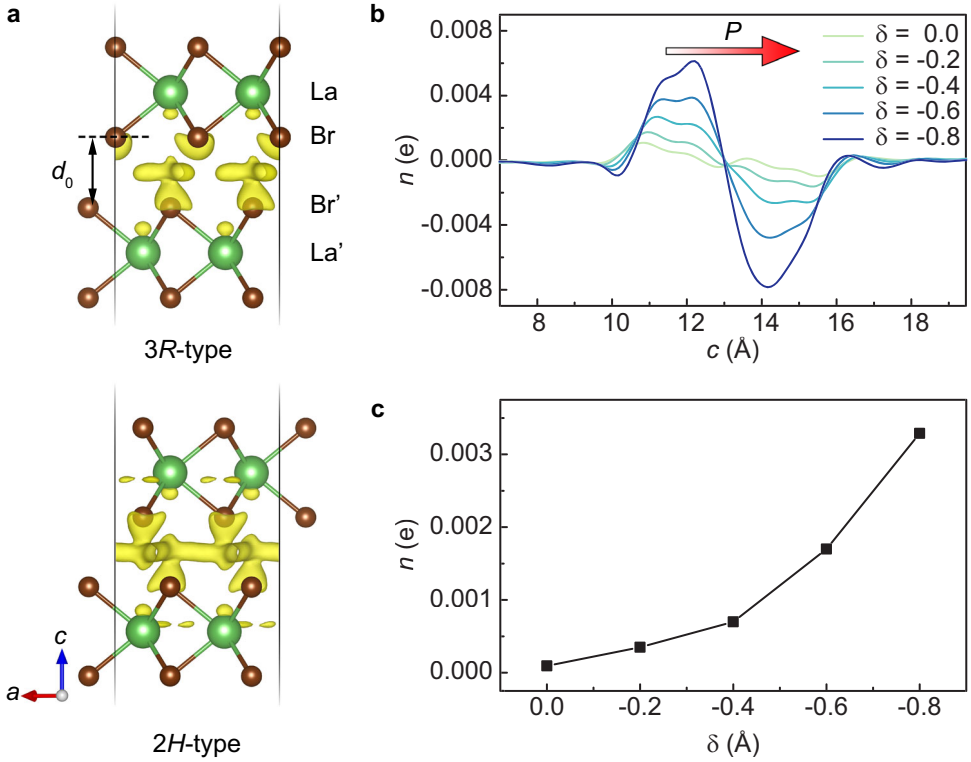

Fig. 3 The electron transfer of bilayer $LaBr_2$. **a** Charge accumulation after stacking those two $LaBr_2$ layers in 3 *R* and 2*H* stacking. The total differential electron along the *c*-axis (**b**) and interlayer transferred charge number (**c**) are calculated by integrating the differential charge at different δ values in 3 *R* stacking.

interlayer sliding of an in-plane translation for polarization reversion induces an interlayer FM-AFM-FM phase transition, as shown in Fig. 2b. Such a magnetic phase transition was a result of competition of FM and AFM superexchange, which enables the manipulation of magnetism through manipulation of overall the interlayer exchange coupling. Based on the fact that both magnetism and polarization are sensitive to the variations of interlayer spacing, we investigated the compressive vertical strains effect on magnetization and polarization by changing the interlayer distance of two $LaBr_2$ layers in 3 *R* stacking, as displayed in Fig. 2c–e. The changing of the interlayer distance $\delta = d - d_0$, where d and d_0 are the strained and equilibrium interlayer distances, will drive the bilayer $LaBr_2$ transition from FM to AFM accompanied by a significant enhancement in out-of-plane polarization. In contrast, the compressive vertical strains applied on 2*H*-type stacking will not change the AFM ordering, demonstrating that the stable AFM exchange of 2*H* type, as shown in Supplementary Fig. 2.

It is imperative to reveal the coupling mechanism between ferromagnetism and ferroelectricity in 3*R*-type $LaBr_2$ bilayer, which is the key of instruction for design superior 2D multiferroic system with robust magnetoelectric coupling. As the charge accumulation after stacking those two $LaBr_2$ layers in Fig. 3a shows, in 3 *R* stacking, the La The above results indicates atoms in the upper layer sit above the Br′ atoms in the lower layer, while the Br atoms in the upper layer lay above the empty site at the centre of the triangle in the lower layer. Such the atomic arrangement allows La-d_z^2 and Br′-p_z orbitals to overlapping, and the accumulated electrons surrounded Br′ atoms, thereby generating an electric dipole moment along the positive *z* direction. Due to the reduce of layer distance, the orbitals overlapping and electric dipole moment increase, as shown in Fig. 3b, c. Note that charge transfer also exists in 2*H* type stacking (see Fig. 3a), but the resulted dipoles cancel each other out due to structural inversion symmetry. In addition, strain-enhanced orbital overlapping in 3*R*-type $LaBr_2$ bilayer allows the Br′-mediated La′-Br′-La AFM superexchange to dominate interlayer exchange, then leading to the FM-AFM phase transition. Clearly, in the present stacking-engineered multiferroic system, the strong magnetoelectric coupling effect occurs due to the synchronized changes of magnetism and polarization under compressive vertical strains, which are different from the conventional type-I and type-II multiferroics.

Spin dynamics of frustrated bimerons in stacking engineered multiferroic $LaBr_2$

Besides the tuning in the long-range magnetic ordering, controlling of short-range spin texture is a superior form of magnetoelectric coupling. Since the value of in-plane nearest and next-nearest exchange interaction parameters in both 2*H* and 3 *R* stacked $LaBr_2$ bilayers are ferromagnetic (positive) and antiferromagnetic (negative) coupling, respectively, as shown in Table 1, indicating that topological spin textures may be induced by frustrated exchange interactions[53,54]. We performed atomically spin dynamics simulation based on Landau-Lifshitz-Gilbert equation on a 100×100 supercell with periodic boundary condition. Figure 4a–c show the spin textures under the layer spacing, which is generated by relaxing the spin configurations from random states. All magnetic frustrated samples exhibit topologically protected bimerons with topological charge $Q = \pm 1$. When δ ranges from −0.4 to 0 Å, the interlayer coupling J_L is relatively weak. The isolated bimerons are distributed randomly in the presence of upper or lower layers and then lead to a nonuniform magnetization instead of a bimeron in the adjacent layer, as shown in Fig. 4a. When the δ decreasing from −0.4 to −0.6 Å and the interlayer exchange coupling transits from FM to AFM in Fig. 4b, this also results in isolated bimerons and a nonuniform magnetization. However, when δ decreases to −0.8 Å, due to the

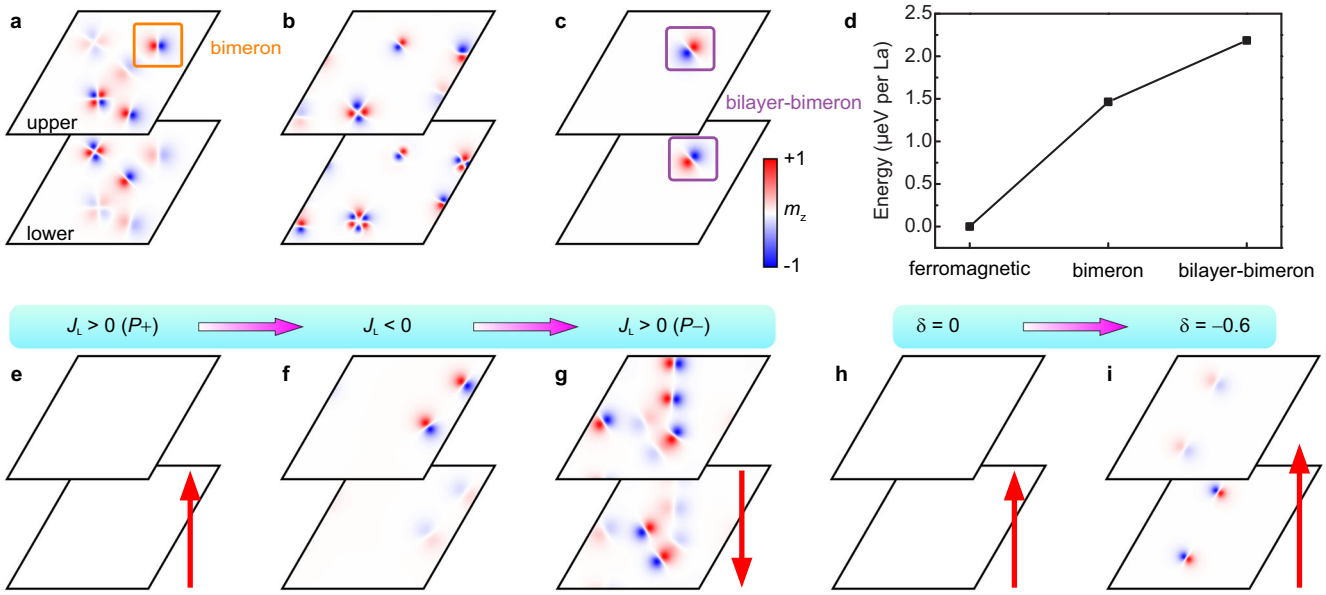

Fig. 4 Frustrated bimeron texture in 3 *R* $LaBr_2$ bilayer. a–c represent the spin texture of $\delta = -0.4$~0, $\delta = -0.6$, and $\delta = -0.8$ Å in $LaBr_2$ with polarization along positive *z* direction, respectively. **d** is the relative energy of FM, bimeron, and bilayer-bimeron states. **e–g** and **h–i** are spin texture evolution from FM initial state caused by polarization inversion and enhancement, respectively.

further enhanced J_L, a pair of antiferromagnetic coupling bimerons appear in the both upper and lower layers (so called bilayer-bimeron), as shown in Fig. 4c. In addition, for the 2*H* stacking phase, we found that the spin texture is essentially identical with that of the 3*R*-type with $\delta = -0.8$ Å, since a strong J_L always exists in 2*H* stacking at the range of $\delta = -0.8 \sim 0$ Å. The spin textures with different δ values in 2*H* and 3 *R* stacking are shown in Supplementary Fig. 3.

As already discussed, enhanced and reversed polarization will modify interlayer exchange coupling J_L, thus, the bilayer system cannot retain the previous magnetic state and subsequent spin rearrangement will be triggered during the energy dissipative process of spin relaxation. As shown in Fig. 4d, we calculated the total energy of the FM state, isolated bimeron with FM background, and the bilayer-bimeron with FM background, and the results show that the FM state is the most stable, while the FM backgrounds with isolated bimeron and bilayer-bimeron states are metastable. Here, we use the FM ordering as the initial magnetic state for spin relaxation of system. Notably, unlike the scenario that the accessible topological spin texture was obtained by the relaxation of the random state, we consider the FM state as the initial magnetic state to investigate the effect of polarization on the spin texture. Figure 4e–g show that the FM-AFM-FM phase transition are caused by polarization reversal. When the ferroelectric polarization transits to the intermediate state with the J_L sign becomes negative, due to the same initial FM orderings of the upper and lower layers, the spin spiral configurations occur in the same position of two layers during the spin relaxed process, thus leading to bimeron in one layer or in the identical positions of two layers as the bilayer-bimeron form. Since the bilayer-bimeron endows with higher energy, the bimeron tends to appear only in one layer of the $LaBr_2$ HS while the other layer remains in FM state, as shown in Fig. 4f. Subsequently, J_L sign returns to a positive value when the polarization switches to another steady state, the bimeron texture breaks the consistency of the spin in the upper and lower layers during the relaxed process, allowing it to appear in anywhere of the bilayer $LaBr_2$, as shown in Fig. 4g. In addition, we also corroborate that when polarization is enhanced caused by the vertical strain, and the result is similar to that of the polarization reversed, as shown in Fig. 4h, i. The above results show that the reversal or enhancement of polarization can excite frustrated bimeron from long-range magnetic ordering, exhibiting a strong coupling effect of mechanical force, electric polarization, and magnetism.

Evolution of polarization texture and spin texture of twisted $LaBr_2$ bilayer moiré superlattice

With identifying the 3*R*-type $LaBr_2$ multiferroics and the understanding of the stacking dependence of interlayer interactions in the bilayers, we now turn to the study of possible spin and polar textures in $LaBr_2$ bilayers with small twist angles. For 3*R*-type $LaBr_2$ bilayers, a long-period moiré pattern can be created by a small twisting or strain between the layers, as seen in Fig. 5a. The moiré periodicity is approximately $A \approx a/\sqrt{\sigma^2 + \theta^2}$ for a small lattice mismatch σ and/or twisting angle θ, where a is the lattice constant of the monolayer. The relevance illustrates that moiré periodicity A increases as the relative twisting or strain between the layers decreases. For small twist angles, the stacking order at any local region in the moiré pattern can be obtained by translating the upper layer of the $LaBr_2$ bilayer by the vector $r = \eta a_1 + \nu a_2$, where $\eta, \nu \in [0, 1]$, and a_1 and a_2 are the lattice vectors of the unit cell. In one moiré cycle, the local regions R_0, R_1, R_2 stacking configuration corresponds to the upper lateral shift $r = \{a_1 + a_2, \frac{1}{3}a_1 + \frac{1}{3}a_2, \frac{2}{3}a_1 + \frac{2}{3}a_2\}$ with respect to lower layer, among which the R_0 configuration possesses an inversion symmetry without polarization value, while the R_1 and R_2 configurations are two different polarization states of the 3 *R* stacking above, respectively, as shown in Fig. 5a. The moiré field is extracted from the stacking-dependent interlayer interaction in these bilayers[39–41], which can be achieved by performing DFT calculations (see Supplementary Materials).

Figure 5b shows the polar texture of moiré superlattices evolved from 3*R*-type stacking. The domains with staggered polarization are formed due to the simultaneous generation of stacking configurations with opposite polarization states upon small twisting angles. According to the relationship between moiré periodicity and twisting angles, the polarization domain density enhances as the twisting angle increase. We also calculated the moiré lattice of 2*H*-type $LaBr_2$ (see Supplementary Fig. 4), however, our results proving that the polarization cannot be induced by a small twisting angle, since any local region of the system remains its central inversion symmetry, as shown in Fig. 5e, f.

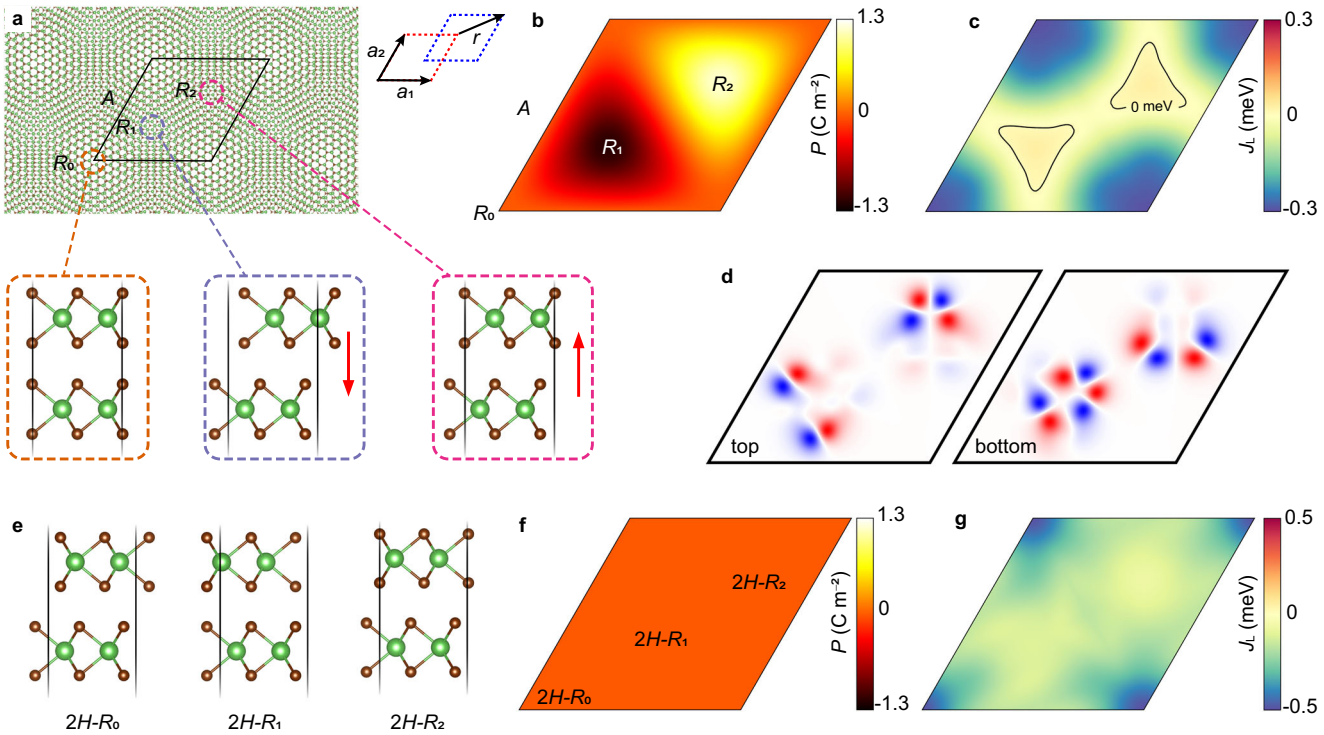

Fig. 5 The moiré pattern of $LaBr_2$ bilayer at small twisting angle. a The moiré superlattice of 3*R*-type $LaBr_2$ bilayer from twisting. Three local regions R_0, R_1, R_2 stacking configuration are amplified to show their different interlayer configurations in the moiré superlattice. **b**, **c** represent polarization and interlayer exchange interaction textures in 3*R*-type $LaBr_2$ moiré superlattice, respectively. **d** is the magnetic texture at the twisting angle $\theta = 0.57°$. **e** is the local regions R_0, R_1, R_2 stacking configuration for 2*H*-type moiré superlattice, and the polarization (**f**) and interlayer exchange (**g**) texture formed in the 2*H*-type moiré superlattice.

According to previous discussion, different kinds of stacking configurations have little effect on the intralayer exchange interaction in terms of the magnetic exchange coupling, while it is particularly sensitive to the interlayer exchange coupling. This is because that the relative twisting between $LaBr_2$ bilayers shifts the interlayer double exchange path, enabling it to locally display a strong AFM coupling or weak ferromagnetic coupling as shown in Fig. 1e. Therefore, this offers the possibility of uneven magnetization textures in the system. Here, we calculated the interlayer coupling constants of 3*R*- and 2*H*-type $LaBr_2$ moiré superlattices, as shown in Fig. 5c, f. Among which, for 3*R*-type moiré superlattice, the interlayer coupling near the R_1, R_2 configurations exhibits weak ferromagnetism, while in R_0 region, it is antiferromagnetic coupling. We performed micromagnetic simulations for the moiré superlattices with a twisting angle $\theta = 0.57°$, as shown in Fig. 5d. For the non-polar R_0 region, the magnetic configuration is a unified interlayer AFM ordering. In contrast, near the R_1 and R_2 configurations, the density of magnetic bimerons increases, owing to the strong interlayer magnetic coupling in the R_0 region where it is not conducive to the survival of bimeron, thus, bimerons can only aggregate to the weakly interlayer coupled R_1 and R_2 regions under the influence of the moiré potential. This leads to the formation of multimeron states[20,54,55], corresponding to ferroelectric domains. Notably, unlike the case where the polarization domain size varies with the size of superlattice, bimeron size (about 8 nm) is immune to the size of superlattice, but depends on local exchange interactions and can be easily affected by the adjacent spin configuration (shown in Supplementary Fig. 3). The above results indicate that there is also a strong magnetoelectric coupling in the moiré superlattice. On the other hand, for 2*H*-type, the interlayer coupling is reduced near the R_1 and R_2, but the overall AFM coupling still remains. It should be noted that although the bimeron can also be stabilized around the R_1, R_2 region, the moiré lattice structures of 2*H*-type are completely different with the 3*R*-type. Polarization domains and magnetic textures underline the significant discrepancy in stack-engineered multiferroics between twisted and non-twisted systems, providing theoretical guidance for twist multiferroics engineering of two-dimensional vdW systems.

Spin dynamics of bilayer bimeron

Topological spin texture can be used as information carriers in future advanced memories. However, there exists an obstacle known as the skyrmion Hall effect, that is, the bimeron trajectories deviate away from the driving current direction due to the Magnus force[26]. One solution for this problem is to fabricate synthetic antiferromagnets, formed by considering two perpendicularly magnetized FM sublayers strongly coupled via the AFM exchange interaction separated by a metallic layer, where skyrmion Hall effect can be completely suppressed[56–58]. Intriguingly, our bilayer $LaBr_2$ can naturally eliminate the effect of the skyrmion Hall effect without the need to construct artificial synthetic antiferromagnets consisting a nonmagnetic layer sandwiched by two magnetic layers. The calculated results show that bilayer-bimeron has four forms when interlayer FM ($J_L > 0$) and AFM ($J_L < 0$) exchange are considered, as shown in Fig. 6a–d. Although the out-of-plane components of the magnetic moments m_z of the upper and lower layers can be aligned in the same or opposite direction and not need to satisfy the most energetically favourable configurations in Fig. 6b, d, while bilayer-bimeron can be stabilized in $LaBr_2$ due to the in-plane magnetic component satisfying of J_L.

The current-driven motion of a rigid bimeron is described by a modified Thiele's equation[59,60]:

$$\mathbf{G} \times \mathbf{v} - \alpha \mathcal{D} \cdot \mathbf{v} + 4\pi \mathcal{B} \cdot \mathbf{j} = 0 \quad (2)$$

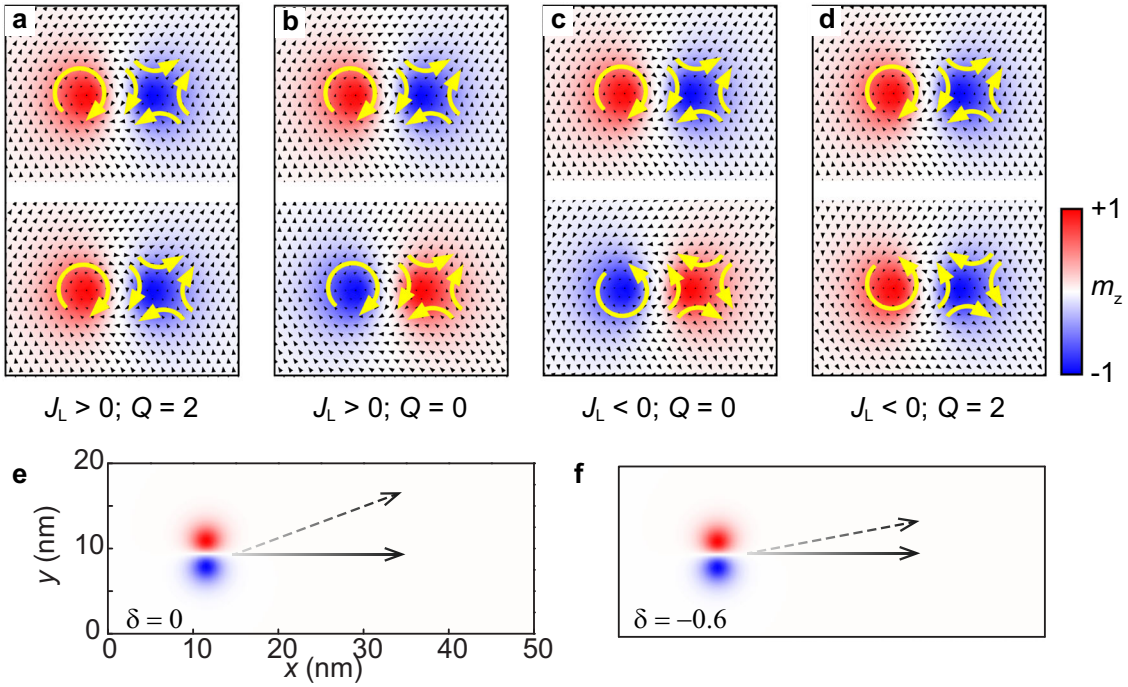

Fig. 6 The bilayer-bimeron texture in 3 *R* $LaBr_2$ bilayer. a–d is the four combination forms of bilayer-bimeron. **e**, **f** represent the top view of the system with $\delta = 0$ ($J_L > 0$) and $\delta = -0.6$ ($J_L < 0$), respectively. The solid and dotted line represent the trajectory of bilayer bimeron with $Q = 0$ and $Q = 2$ respectively.

where $\mathbf{G} = (0, 0, -4\pi Q)$ is the gyromagnetic coupling vector, α is the magnetic damping parameter and $\mathcal{D}$ is the dissipative force tensor. $\mathcal{B}$ is the tensor relating to the driving force. $v = (v_x, v_y)$ is the propagation velocity along the x and y axis, respectively. Among them, the topological Hall effect is included in the Magnus force of the first term in Eq. 2, which is proportional to the topological charge Q. The Thiele equation yields $v_x = \left[-\alpha\mathcal{D}/\left(Q^2 + \alpha^2\mathcal{D}^2\right)\right]\mathcal{B}j$ and $v_y = \left[Q/\left(Q^2 + \alpha^2\mathcal{D}^2\right)\right]\mathcal{B}j$ for the velocity components of bimeron along x and y direction. In Fig. 6b, c, the opposite Q signs result in the opposite transverse motion v_y of bimeron in the upper and lower layers, leading the bilayer-bimeron moves horizontally. Particularly, the positive J_L value in Fig. 6b allows bilayer-bimeron to naturally suppress the skyrmion Hall effect in the FM background without resorting to any external fields. And for the bilayer-bimeron with topological number $Q = 2$ in Fig. 6a, c, the trajectory will be shifted under the influence of skyrmion Hall effect. We performed a simulation that the bilayer-bimeron was driven by current on the non-twisted 3 *R* $LaBr_2$ system. The systems with $\delta = 0$ and $\delta = -0.6$ are adopted to simulate the scenario of bilayer-bimeron configurations with $J_L > 0$ and $J_L < 0$, respectively. As expected, the bilayer-bimeron with opposite topological numbers can move parallelly in nanoribbon, as shown in Fig. 6e.

DISCUSSION

In summary, using first-principle calculations, we designed a multiferroic system by using the twisted stack engineering of 2D magnetic layers. The 3 *R* stacked $LaBr_2$ create out-of-plane spontaneous ferroelectricity due to the broken inversion symmetry. Such a polarization can be reversed by a slight interlayer sliding, which is equivalent to an energy barrier of 14.81 meV per unit. The interlayer weak FM is highly sensitive to the stacking distance. Therefore, the enhancement and reversal of polarization will trigger magnetic phase transition, which makes the 3 *R* stacked $LaBr_2$ exhibit strong magnetoelectric coupling effects. Spin dynamics simulations show that such magnetoelectric coupling-induced magnetic phase transition can excite topologically protected bimeron from long-range magnetic orderings. Moreover, the topological Hall effect can be suppressed in ferromagnetically or antiferromagnetically exchange-coupled bilayer-bimeron system by counteracting the Magnus forces in the upper and lower layers. We also calculated the moiré pattern with small twisting angles of the 3 *R* bilayer $LaBr_2$, where the small twisting of the stacked multiferroic system results in staggered polarization domains and an uneven spatial distribution of magnetic topological textures. Our work points the direction for the design of superior multiferroics with strong magnetoelectric coupling.

METHOD

The DFT method

Magnetic parameters and electronic structure were calculated by performing first-principle simulations within the DFT[61,62], using the projected augmented wave pseudopotentials method as implemented in the Vienna Ab-initio Simulation Package (VASP)[63,64]. The exchange correlation energy is calculated within the generalized gradient approximation (GGA) of Perdew-Burke-Ernzerhof form[65]. Due to that, the GGA algorithm will underestimate the bandgap of the *f* orbitals, an effective 5 eV Hubbard U_{eff} parameter is applied on La's *f* orbitals using the Dudarev method in order to correct its bandgap and prevents *f* orbitals from participating in orbital hybridization near the Fermi level[66]. The plane wave cutoff energy was set to 500 eV and the van der Waals interaction is included by the semiempirical DFT-D3 method[67]. We utilized a centered $18 \times 18 \times 1$ Monkhorst-Pack *k*-point mesh for calculating properties of $LaBr_2$. Utilizing the conjugate gradient method, the plane lattice constant and atomic coordinates are fully relaxed until the energy and force converge to 10^{-5} eV and 10^{-2} eV $Å^{-1}$, respectively. In order to eliminate the periodic boundary effect, a 15 Å thin vacuum layer is introduced along the *z* direction. Spin-orbit coupling is used to calculate magnetocrystalline anisotropy. In the $LaBr_2$ moiré superlattice, the interlayer exchange constant was parametrized by evaluating the energy on a grid of points for an $LaBr_2$ bilayer, the upper layer of $LaBr_2$ is shifted relative to the lower layer over a 6×6 grid in the unit cell to sample the entire moiré range. The

in-plane positions of all atoms in the bilayer are fixed during optimization, but they are allowed to relax in the out-of-plane direction.

Micromagnetic simulations

Using *Spirit* package to simulate the spin dynamics of $LaBr_2$ bilayer[68], the time evolution of the magnetization is described by the LLG equation[69,70], it can be written as:

$$\frac{\partial \mathbf{m}_i}{\partial t} = -\frac{\gamma}{(1+\alpha^2)\mu_i}\mathbf{m}_i \times \mathbf{B}_i^{\mathrm{eff}}(t) - \frac{\gamma\alpha}{(1+\alpha^2)\mu_i}\mathbf{m}_i \times \left[\mathbf{m}_i \times \mathbf{B}_i^{\mathrm{eff}}(t)\right] - \frac{\alpha-\beta}{(1+\alpha^2)}u\mathbf{m}_i \times \left(\hat{\mathbf{j}}\cdot\nabla\right)\mathbf{m}_i + \frac{1+\beta\alpha}{(1+\alpha^2)}u\mathbf{m}_i \times \left[\mathbf{m}_i \times \left(\hat{\mathbf{j}}\cdot\nabla\right)\mathbf{m}_i\right] \tag{3}$$

where γ is the electron gyromagnetic ratio, $\alpha = 0.05$ is the damping parameter, $\beta = 0.01$ is a nonadiabaticity parameter, $u = jPg\mu_B/(2eM_s)$ with current density j, P is the polarization of the current, e is the electron charge, M_s is the saturation magnetization. $\hat{\mathbf{j}} = \boldsymbol{x}$ denotes the electron current normal vector, and $\nabla = \partial/\partial\mathbf{r}$ is the spatial gradient acting on the spin orientation.

For discrete lattice, the topological charge Q is calculated using the definition of Berg and Lüscher[71], and arrive at the following expression:

$$Q = \frac{1}{4\pi}\sum_l A_l \tag{4}$$

with

$$cos\left(\frac{A_l}{2}\right) = \frac{1+\mathbf{m}_i\cdot\mathbf{m}_j+\mathbf{m}_j\cdot\mathbf{m}_k+\mathbf{m}_k\cdot\mathbf{m}_i}{\sqrt{2\left(1+\mathbf{m}_i\cdot\mathbf{m}_j\right)\left(1+\mathbf{m}_j\cdot\mathbf{m}_k\right)\left(1+\mathbf{m}_k\cdot\mathbf{m}_i\right)}} \tag{5}$$

where l runs over all elementary triangles of any triangulated regular lattice and A_l is the solid angle formed by the three spin vectors $\mathbf{m}_i$, $\mathbf{m}_j$ and $\mathbf{m}_k$ of the lth triangle. The sign of A_l is determined as $\mathrm{sign}(A_l) = \mathrm{sign}\left[\mathbf{m}_i\cdot\left(\mathbf{m}_j\times\mathbf{m}_k\right)\right]$. Note that the triangles should cover all lattice area with no overlap and $\mathbf{m}_i$, $\mathbf{m}_j$ and $\mathbf{m}_k$ should be anticlockwisely ordered.

Monte Carlo simulations

The magnetic phase transitions of $LaBr_2$ bilayer determined by performing Monte Carlo simulations with a $100\times100\times1$ supercell based on the Heisenberg model of Eq. 1. For each temperature, the initial 10^5 Monte Carlo steps were discarded for equilibrium consideration and additional 10^5 Monte Carlo steps were retained for statistical averaging of the simulation. The critical temperature is estimated by the peak position of the specific heat (C), which is defined as

$$C = \frac{\left(\langle E^2\rangle - \langle E^2\rangle\right)}{k_B T^2} \tag{6}$$

where E is the thermal energy, k_B is Boltzmann constant, and T is temperature.

DATA AVAILABILITY

The data that support the findings of this study are available from the corresponding authors upon reasonable request.

Received: 15 February 2022; Accepted: 13 June 2022;
Published online: 22 July 2022

REFERENCES

1. Ikeda, S. et al. Magnetic tunnel junctions for spintronic memories and beyond. *IEEE Trans. Electron Devices* **54**, 991–1002 (2007).
2. Uchino, K. *Ferroelectric devices* (CRC press, 2018).
3. Shimada, T., Uratani, Y. & Kitamura, T. Vacancy-driven ferromagnetism in ferroelectric $PbTiO_3$. *Appl. Phys. Lett.* **100**, 162901 (2012).
4. Hill, N. A. Why are there so few magnetic ferroelectrics? *J. Phys. Chem. B* **104**, 6694–6709 (2000).
5. Novoselov, K. S. et al. Electric field effect in atomically thin carbon films. *Science* **306**, 666–669 (2004).
6. Ding, W. et al. Prediction of intrinsic two-dimensional ferroelectrics in In_2Se_3 and other III_2-VI_3 van der Waals materials. *Nat. Comm.* **8**, 14956 (2017).
7. Gibertini, M., Koperski, M., Morpurgo, A. & Novoselov, K. Magnetic 2D materials and heterostructures. *Nat. Nanotech.* **14**, 408–419 (2019).
8. Geim, A. K. & Grigorieva, I. V. Van der Waals heterostructures. *Nature* **499**, 419–425 (2013).
9. Novoselov, K., Mishchenko, O. A., Carvalho, O. A. & Neto, A. C. 2D materials and van der Waals heterostructures. *Science* **353**, aac9439 (2016).
10. Yao, X., Wang, Y. & Dong, S. Noncollinear topological textures in two-dimensional van der Waals materials: from magnetic to polar systems. *Int. J. Mod. Phys. B* **35**, 2130004 (2021).
11. Liu, Y. et al. Van der Waals heterostructures and devices. *Nat. Rev. Mater.* **1**, 16042 (2016).
12. Gong, C., Kim, E. M., Wang, Y., Lee, G. & Zhang, X. Multiferroicity in atomic van der Waals heterostructures. *Nat. Comm.* **10**, 2657 (2019).
13. Yin, L. & Parker, D. S. Out-of-plane magnetic anisotropy engineered via band distortion in two-dimensional materials. *Phys. Rev. B* **102**, 054441 (2020).
14. Xue, F., Wang, Z., Hou, Y., Gu, L. & Wu, R. Control of magnetic properties of $MnBi_2Te_4$ using a van der Waals ferroelectric III_2-VI_3 film and biaxial strain. *Phys. Rev. B* **10**, 184426 (2020).
15. Sun, W. et al. Controlling bimerons as skyrmion analogues by ferroelectric polarization in 2D van der Waals multiferroic heterostructures. *Nat. Comm.* **11**, 5930 (2020).
16. Li, C.-K., Yao, X.-P. & Chen, G. Writing and deleting skyrmions with electric fields in a multiferroic heterostructure. *Phys. Rev. Res.* **3**, L012026 (2021).
17. Bogdanov, A. N. & Yablonskii, D. Thermodynamically stable "vortices" in magnetically ordered crystals. The mixed state of magnets. *Zh. Eksp. Teor. Fiz.* **95**, 178 (1989).
18. Roessler, U. K., Bogdanov, A. & Pfleiderer, C. Spontaneous skyrmion ground states in magnetic metals. *Nature* **442**, 797–801 (2006).
19. Mühlbauer, S. et al. Skyrmion lattice in a chiral magnet. *Science* **323**, 915–919 (2009).
20. Kharkov, Y., Sushkov, O. & Mostovoy, M. Bound states of skyrmions and merons near the Lifshitz point. *Phys. Rev. Lett.* **119**, 207201 (2017).
21. Huang, X. et al. Interfacial coupling induced critical thickness for the ferroelectric bistability of two-dimensional ferromagnet/ferroelectric van der Waals heterostructures. *Phys. Rev. B* **100**, 235445 (2019).
22. Yasuda, K., Wang, X., Watanabe, K., Taniguchi, T. & Jarillo-Herrero, P. Stacking-engineered ferroelectricity in bilayer boron nitride. *Science* **372**, 1458–1462 (2021).
23. Fei, Z. et al. Ferroelectric switching of a two-dimensional metal. *Nature* **560**, 336–339 (2018).
24. Li, L. & Wu, M. Binary compound bilayer and multilayer with vertical polarizations: two-dimensional ferroelectrics, multiferroics, and nanogenerators. *ACS Nano* **11**, 6382–6388 (2017).
25. Yang, Q., Wu, M. & Li, J. Origin of two-dimensional vertical ferroelectricity in WTe_2 bilayer and multilayer. *J. Phys. Chem. Lett.* **9**, 7160–7164 (2018).
26. Liu, X., Pyatakov, A. P. & Ren, W. Magnetoelectric coupling in multiferroic bilayer VS_2. *Phys. Rev. Lett.* **125**, 247601 (2020).
27. Göbel, B., Mook, A., Henk, J., Mertig, I. & Tretiakov, O. A. Magnetic bimerons as skyrmion analogues in in-plane magnets. *Phys. Rev. B* **99**, 060407 (2019).
28. Kim, S. K. Dynamics of bimeron skyrmions in easy-plane magnets induced by a spin supercurrent. *Phys. Rev. B* **99**, 224406 (2019).
29. Emori, S., Bauer, U., Ahn, S.-M., Martinez, E. & Beach, G. S. Current-driven dynamics of chiral ferromagnetic domain walls. *Nat. Mater.* **12**, 611–616 (2013).
30. Romming, N. et al. Writing and deleting single magnetic skyrmions. *Science* **341**, 636–639 (2013).
31. Jonietz, F. et al. Spin transfer torques in MnSi at ultralow current densities. *Science* **330**, 1648–1651 (2010).
32. Nagaosa, N. & Tokura, Y. Topological properties and dynamics of magnetic skyrmions. *Nat. Nanotech.* **8**, 899–911 (2013).
33. Dean, C. R. et al. Hofstadter's butterfly and the fractal quantum Hall effect in moiré superlattices. *Nature* **497**, 598–602 (2013).
34. Ponomarenko, L. et al. Cloning of Dirac fermions in graphene superlattices. *Nature* **497**, 594–597 (2013).
35. Hunt, B. et al. Massive Dirac fermions and Hofstadter butterfly in a van der Waals heterostructure. *Science* **340**, 1427–1430 (2013).
36. Cao, Y. et al. Correlated insulator behaviour at half-filling in magic-angle graphene superlattices. *Nature* **556**, 80–84 (2018).
37. Cao, Y. et al. Unconventional superconductivity in magic-angle graphene superlattices. *Nature* **556**, 43–50 (2018).
38. Yankowitz, M. et al. Tuning superconductivity in twisted bilayer graphene. *Science* **363**, 1059–1064 (2019).
39. Tong, Q., Liu, F., Xiao, J. & Yao, W. Skyrmions in the Moiré of van der Waals 2D Magnets. *Nano Lett.* **18**, 7194–7199 (2018).
40. Xiao, F., Chen, K. & Tong, Q. Magnetization textures in twisted bilayer CrX_3 (X = Br, I). *Phys. Rev. Res.* **3**, 013027 (2021).

41. Akram, M. et al. Moiré skyrmions and chiral magnetic phases in twisted CrX_3 (X = I, Br, and Cl) bilayers. *Nano Lett.* **21**, 6633–6639 (2021).
42. Krämer, K., Schleid, T., Schulze, M., Urland, W. & Meyer, G. Three bromides of lanthanum: $LaBr_2$, $La2Br_5$, and $LaBr_3$. *Z. Anorg. Allg. Chem.* **575**, 61–70 (1989).
43. Zhao, P. et al. Single-layer $LaBr_2$: Two-dimensional valleytronic semiconductor with spontaneous spin and valley polarizations. *Appl. Phys. Lett.* **115**, 261605 (2019).
44. Jiang, Z., Wang, P., Xing, J., Jiang, X. & Zhao, J. Screening and design of novel 2D ferromagnetic materials with high Curie temperature above room temperature. *ACS Appl. Mater. Interfaces* **10**, 39032–39039 (2018).
45. McGuire, M. A., Dixit, H., Cooper, V. R. & Sales, B. C. Coupling of crystal structure and magnetism in the layered, ferromagnetic insulator CrI_3. *Chem. Mater.* **27**, 612–620 (2015).
46. Jang, S. W., Jeong, M. Y., Yoon, H., Ryee, S. & Han, M. J. Microscopic understanding of magnetic interactions in bilayer CrI_3. *Phys. Rev. Mater.* **3**, 031001 (2019).
47. Marzari, N., Mostofi, A. A., Yates, J. R., Souza, I. & Vanderbilt, D. Maximally localized Wannier functions: theory and applications. *Rev. Mod. Phys.* **84**, 1419 (2012).
48. Kanamori, J. Crystal distortion in magnetic compounds. *J. Appl. Phys.* **31**, S14–S23 (1960).
49. Goodenough, J. B. Theory of the role of covalence in the perovskite-type manganites [La, M (II)] MnO_3. *Phys. Rev.* **100**, 564 (1955).
50. Anderson, P. W. New approach to the theory of superexchange interactions. *Phys. Rev.* **115**, 2 (1959).
51. Huang, B. et al. Layer-dependent ferromagnetism in a van der Waals crystal down to the monolayer limit. *Nature* **546**, 270–273 (2017).
52. Mills, G., Jónsson, H. & Schenter, G. K. Reversible work transition state theory: application to dissociative adsorption of hydrogen. *Surf. Sci.* **324**, 305–337 (1995).
53. Zhang, X. et al. Skyrmion dynamics in a frustrated ferromagnetic film and current-induced helicity locking-unlocking transition. *Nat. Comm.* **8**, 1717 (2017).
54. Zhang, X. et al. Static and dynamic properties of bimerons in a frustrated ferromagnetic monolayer. *Phys. Rev. B* **101**, 144435 (2020).
55. Kuchkin, V. M. & Kiselev, N. S. Turning a chiral skyrmion inside out. *Phys. Rev. B* **101**, 064408 (2020).
56. Zhang, X., Zhou, Y. & Ezawa, M. Magnetic bilayer-skyrmions without skyrmion Hall effect. *Nat. Comm.* **7**, 10293 (2016).
57. Zhang, X., Ezawa, M. & Zhou, Y. Thermally stable magnetic skyrmions in multilayer synthetic antiferromagnetic racetracks. *Phys. Rev. B* **94**, 064406 (2016).
58. Zhou, S., Wang, C., Zheng, C. & Liu, Y. Manipulating skyrmions in synthetic antiferromagnetic nanowires by magnetic field gradients. *J. Magn. Magn. Mater.* **493**, 165740 (2020).
59. Jiang, W. et al. Direct observation of the skyrmion Hall effect. *Nat. Phys.* **13**, 162–169 (2017).
60. Thiele, A. Steady-state motion of magnetic domains. *Phys. Rev. Lett.* **30**, 230 (1973).
61. Hohenberg, P. & Kohn, W. Inhomogeneous electron gas. *Phys. Rev.* **136**, B864 (1964).
62. Kohn, W. & Sham, L. J. Self-consistent equations including exchange and correlation effects. *Phys. Rev.* **140**, A1133 (1965).
63. Kresse, G. & Hafner, J. Ab initio molecular dynamics for liquid metals. *Phys. Rev. B* **47**, 558 (1993).
64. Kresse, G. & Furthmüller, J. Efficient iterative schemes for ab initio total-energy calculations using a plane-wave basis set. *Phys. Rev. B* **54**, 11169 (1996).
65. Perdew, J. P., Burke, K. & Ernzerhof, M. Generalized gradient approximation made simple. *Phys. Rev. Lett.* **77**, 3865 (1996).
66. Dudarev, S., Botton, G., Savrasov, S., Humphreys, C. & Sutton, A. Electron-energy-loss spectra and the structural stability of nickel oxide: An LSDA+U study. *Phys. Rev. B* **57**, 1505 (1998).
67. Grimme, S., Antony, J., Ehrlich, S. & Krieg, H. A consistent and accurate ab initio parametrization of density functional dispersion correction (DFT-D) for the 94 elements H-Pu. *J. Chem. Phys.* **132**, 154104 (2010).
68. Müller, G. P. et al. Spirit: Multifunctional framework for atomistic spin simulations. *Phys. Rev. B* **99**, 224414 (2019).
69. Landau, L. & Lifshitz, E. On the theory of the dispersion of magnetic permeability in ferromagnetic bodies. *Phy. Z. Sowjetunion* **8**, 153 (1935).
70. Gilbert, T. L. A phenomenological theory of damping in ferromagnetic materials. *IEEE Trans. Magn.* **40**, 3443–3449 (2004).
71. Berg, B. & Lüscher, M. Definition and statistical distributions of a topological number in the lattice O (3) σ-model. *Nucl. Phys. B* **190**, 412–424 (1981).

ACKNOWLEDGEMENTS

We acknowledge grants from the National Natural Science Foundation of China under research (Nos. 52102238, 51571083, and 11674083) and Henan University (No. CX3040A0950115, CJ3050A0670499, CJ3050A0670524). H.L. acknowledges the support from the National Natural Science Foundation of China (Grant No. 11804078) and Henan University (Grant No. CJ3050A0240050). Z.X.C. thanks Australia Research Council for support (DP190100150).

AUTHOR CONTRIBUTIONS

Z.X.C. conceived the idea. W.S., W.X.W., Z.X.C., and H.L. carried out the calculation and analysis of the result. W.S., W.X.W., Z.X.C., and H.L. wrote the paper. W.S. and W.X.W. are listed as co-first author. All authors contribute the comments on the paper.

COMPETING INTERESTS

The authors declare no competing interests.

ADDITIONAL INFORMATION

Supplementary information The online version contains supplementary material available at https://doi.org/10.1038/s41524-022-00833-4.

Correspondence and requests for materials should be addressed to Hang Li or Zhenxiang Cheng.

Reprints and permission information is available at http://www.nature.com/reprints

Publisher's note Springer Nature remains neutral with regard to jurisdictional claims in published maps and institutional affiliations.